FLUID FLOW OBSERVATIONS OF THE SPRAY NEAR-FIELD USING HIGH-SPEED X-RAY IMAGING

Julie K. Bothell,[1] Timothy B. Morgan,[1] Alan L. Kastengren,[2] & Theodore J. Heindel[1,]*

[1]*Center for Multiphase Flow Research and Education and Department of Mechanical Engineering, Iowa State University, Ames, Iowa, USA*

[2]*X-Ray Science Division, Advanced Photon Source, Argonne National Laboratory, Lemont, IL, USA*

*Address all correspondence to: Theodore J. Heindel, Department of Mechanical Engineering, Iowa State University, Ames, IA, 50011-2161, USA; Tel.: +1-515-294-0057; Fax: +1-515-294-3261, E-mail: theindel@iastate.edu

Sprays are important to many industrial processes, but the near-field region where spray formation takes place is difficult to visualize and characterize through visible light imaging because this region is typically optically dense. X-ray imaging is one technique that can penetrate this optically dense region and provide unique observations of the spray formation process. This study uses high-speed white beam X-ray imaging conducted at the Advanced Photon Source to capture spray formation dynamics from a canonical airblast atomizer. A range of momentum flux ratios are visualized by varying the gas flow rate while the liquid flow rate is held constant. The X-rays show overlapping flow structures including bags, ligaments, mushrooms, and webs. Air bubbles are captured within the liquid regions, and a very dynamic crown forms at the liquid needle exit at higher momentum flux ratios. Finally, at the highest momentum flux ratios, air bubbles and liquid droplets are observed migrating upstream in the center of the crown, and this motion is attributed to a toroidal recirculation cell at the nozzle exit.

KEY WORDS: *atomization, high-speed imaging, primary breakup, spray, synchrotron, X-ray diagnostics*

1. INTRODUCTION

Sprays are found in many natural and industrial settings, from rain and breaking ocean waves to liquid fuel combustion and additive manufacturing. In typical applications, when liquid is ejected from a nozzle in a gaseous environment and sufficient shear is available, the liquid is broken up into a liquid–gas spray. The resulting spray is commonly divided into three regions. The near-field region is closest to the nozzle exit and is generally composed of a dense liquid core or sheet that undergoes breakup into ligaments, which then undergo additional breakup into individual liquid droplets. The spray mid-field region is usually composed of a dispersion of liquid ligaments undergoing breakup and individual liquid droplets that may undergo secondary breakup. Finally, the far-field region contains a dilute dispersion of individual liquid droplets that con-

tinue to disperse radially and axially as they travel from the nozzle exit. While the far-field region has been well characterized, primary breakup and the near-field region has been minimally investigated because the thick liquid core and large structures render the region nearly impenetrable to visible light. However, the near-field region is vital to understanding sprays because it controls and sets the primary combustion zone for fuel sprays (Lightfoot et al., 2015). Additionally, it provides the initial conditions as the spray enters the secondary breakup region.

The spray mid- and far-field regions can be quantified using optical- and laser-based methods like shadowgraphy, back-illuminated or backlit imaging, Phase Doppler Particle Analysis (PDPA), or particle image velocimetry (PIV) (Bachalo, 2000; Castrejón-Pita et al., 2013; Fansler and Parrish, 2015; Settles and Hargather, 2017). The challenge of using these techniques in the near-field is that the spray is usually optically dense in this region; hence, other techniques are required such as X-ray imaging (Kastengren et al., 2012; Linne, 2012a, 2012b, 2013; Kastengren and Powell, 2014; Heindel, 2018). Unlike visible light, X-rays are able to penetrate the dense liquid near-field region. The X-ray attenuation (absorption) in this dense region is related to the amount and density of material through which the beam passes. The attenuation can be used to quantity the amount of material present in the line of sight along the X-ray beam using Beer-Lambert's Law (Li et al., 2019). One additional advantage of X-rays is the slight refraction and diffraction at liquid–gas interfaces, which can actually enhance visualization in a technique called phase contrast imaging (Kastengren et al., 2012; Heindel, 2018).

Traditional radiography is the act of obtaining a shadow-like image of an object using penetrating radiation such as X-rays or γ-rays, where darker regions correspond to where the object is more dense and/or thicker (Cartz, 1995); a simple medical X-ray showing bone structure is a radiograph. X-ray computed tomography is when radiographs of an object are acquired from several hundred viewing directions and then reconstructed with standard algorithms to show intensity variations of the object cross-section (Hsieh, 2003; Hampel, 2015).

X-rays have been used to visualize multiphase flows for many years (Heindel, 2011; Aliseda and Heindel, 2021). They are typically generated using one of two methods: (i) an electron beam hitting a metal target like that found in traditional tube sources, or (ii) a synchrotron light source. The high-speed X-ray imaging in this article was produced using the synchrotron facility at the Advanced Photon Source (APS) at Argonne National Laboratory. X-rays produced by a synchrotron source are polychromatic, like those produced by tube sources, but they are highly collimated and produce a much higher X-ray flux [up to 6 orders of magnitude higher (Matusik et al., 2019)]. X-rays produced with a synchrotron source are found only at selected facilities such as APS (Kastengren et al., 2012; Kastengren and Powell, 2014; Tekawade et al., 2020).

There are several X-ray imaging techniques that can be used to characterize sprays (Heindel, 2018). White beam radiography or white beam imaging can be completed using a synchrotron source. White beam imaging uses the high intensity X-ray beam from the synchrotron that is composed of a range of energies (wavelengths), similar to white light being composed of a range of wavelengths in the visible spectrum. Once the beam passes through the object of interest, it is detected by a scintillator crystal that luminesces

visible light proportional to the amount of absorbed X-ray energy. The luminescence is imaged using a turning mirror into a high-speed digital camera that is shielded from the X-rays. White beam imaging has been used to investigate, for example, the liquid core dynamics of a high momentum ratio spray (Machicoane et al., 2019), the two-phase flow behavior in an opaque beryllium injector (Lin et al., 2017), the mixing of an impinging jet spray (Halls et al., 2017), and the gas–liquid interface of a turbulent liquid jet being injected into still air (Osta et al., 2012).

A subset of white beam imaging is called X-ray phase contrast imaging (XPCI), which requires a high-energy coherent X-ray beam like the white beam at a synchrotron facility. XPCI is based on the differences between the refractive index of a sample and its environment. The X-ray beam passes through the object of interest (i.e., fluid flow) and is allowed to propagate some distance past it. A phase shift is produced at the interface of two materials with a high density difference, such as a gas–liquid interface, creating a Fresnel diffraction pattern that enhances the absorption contrast at the interface; the enhanced absorption contrast can be used to facilitate image analysis to quantify flow features. XPCI has recently been used to explore the flow through a fuel injector (Moon et al., 2015), the cavitation dynamics in a high-speed nozzle (Karathanassis et al., 2021), and venturi flows (Khlifa et al, 2017; Zhang et al., 2020a, 2020b).

Tomographic imaging of multiphase flows has been summarized in recent reviews (Heindel, 2011; Aliseda and Heindel, 2021). This imaging modality has also been applied to sprays. To acquire the necessary number of image projections, either the source and detector have to revolve around the spray (Halls et al., 2014; Li et al., 2017b), the spray has to rotate within the imaging region (Coletti et al., 2014; Tekawade et al., 2020), or multiple source-detector pairs have to be arranged around the spray (Rahman et al., 2018; Halls et al., 2019).

This article describes the flow structures from a canonical airblast atomizer that are visualized using high-intensity X-rays, which allows for high-speed flow visualization (up to 100 kHz in this study). While the liquid flow rate is held constant, the gas flow rate is varied to provide a range of momentum flux ratios, where the shear imposed on the liquid increases with increasing momentum flux ratio, creating highly dynamic aperiodic flows, which are discussed below.

2. EXPERIMENTAL SETUP

The experimental setup for this study consists of two major components, the flow loop (discussed in Section 2.1) and the X-ray imaging setup (discussed in Section 2.3). Additionally, the non-dimensionalized flow parameters are defined in Section 2.2 and a brief discussion on the X-ray image processing can be found in Section 2.4.

2.1 Nozzle and Flow Loop

The spray used in this study is generated using a canonical two-fluid airblast atomizer shown in Fig. 1. The inner aluminum liquid needle has an ID of $d_l = 2.1$ mm and OD of
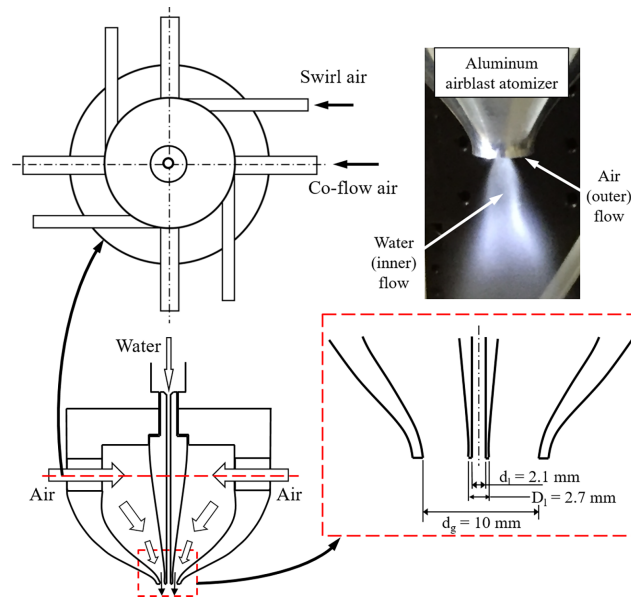
FIG. 1: Airblast atomizer used in this study

D_l = 2.7 mm at the tip, and is coaxial with an outer air chamber (d_g = 10 mm ID at the tip). Two identical outer air chambers are used in this work, one fabricated from aluminum and the other fabricated from acetal plastic. The aluminum outer nozzle allows enough X-ray signal through to view the internal flow [see, for example, Machicoane et al. (2019) for a static image or Li et al. (2017a) for a video]. The acetal plastic nozzle has a precision copper ring at the exit and is used as an electrical grounding path for a separate study involving electrostatics; the copper ring prevents X-ray visualization inside the nozzle. Complete details of the nozzle design are found elsewhere (Machicoane and Aliseda, 2017; Huck et al., 2018; Machicoane et al., 2019).

Air and water are used as the two fluids in the airblast atomizer. The air and water flow loops have been detailed elsewhere (Li et al., 2019; Bothell et al., 2020a) and only a summary is provided here. Compressed air is provided through the building supply and is filtered prior to entering the flow loop. After the filter, the air is partitioned into two lines, each of which has a pressure regulator to limit the air pressure that is fed to the system. One of the compressed air lines is used to feed air to the nozzle, while the second is used to pressurize a water tank to provide the water to the nozzle. A ball valve on each of the air lines closes the air line when not in use.

The air feed line is partitioned a second time to direct the air flow as "co-flow" and "swirl" air (see Fig. 1). Electronic proportioning valves and air flow meters are located after this partition and are used to control and monitor the air flow rates. Each co-flow and swirl air line passes through air flow meters and then each are further split into four identical lines that are then attached to the upper portion of the nozzle to provide air flow into the test nozzle. The four co-flow lines impinge onto the liquid needle longitudinal

axis, across the four quadrants, producing a purely coaxial gas stream at the nozzle exit. The four swirl lines enter the air nozzle in the same plane as the co-flow lines, but tangent to the air nozzle wall, introducing swirl in the gas stream. When swirl is added to the gas, the total gas flow rate remains constant, diverting part of the total gas from the co-flow to the swirl injection.

The second air line is fed into the water tank to create a pressurized section of air on top of the water that provides the force necessary to push the water through the water line. From there, the water passes through a water flow meter and an electronic proportioning valve and then enters the liquid needle. The liquid needle is designed to produce fully developed laminar Poiseuille flow and has $L/d_l \approx 50$.

The electronic proportioning valves and flow meters are connected to a data acquisition system that provides real time measurement and control. The electronic proportioning valves are each controlled by a proportional, integral, and derivative (PID) control system implemented in an in-house LabView program. Values from the flow meters are sent to the data acquisition system and used as feedback, as well as stored so that any observed phenomenon can be related back to the instantaneous flow measurement.

2.2 Flow Parameters

The total liquid (Q_l), co-flow (Q_{NS}), and swirl (Q_{SW}) flow rates are measured during each test, where the total air flow rate $Q_{total} = Q_{NS} + Q_{SW}$. The ratio of swirl air flow rate to co-flow air flow rate is defined as the swirl ratio (SR) to quantify the amount of air entering the gas nozzle through the tangential ports relative to the amount entering perpendicular to the liquid needle:

$$SR = \frac{Q_{SW}}{Q_{NS}} \tag{1}$$

In this work, most observations are provided with SR = 0; a few cases are shown with SR = 1. Note that the total gas flow rate remains constant when the swirl ratio is varied.

The liquid Reynolds number is defined as:

$$Re_l = \frac{U_l d_l}{\nu_l} \tag{2}$$

where U_l is the mean exit velocity of the liquid and ν_l is the kinematic viscosity of water. The gas Reynolds number is defined as:

$$Re_g = \frac{U_g d_{eff}}{\nu_g} = \frac{U_g \sqrt{d_g^2 - D_l^2}}{\nu_g} \tag{3}$$

where U_g is the mean exit velocity of the gas, defined as Q_{total}/A_g with A_g the total gas exit area; ν_g is the kinematic viscosity of air; and d_{eff} is the gas effective diameter at the nozzle exit, defined as the diameter of a circle with the exit area equal to A_g.

The momentum flux ratio is defined as:

$$M = \frac{\rho_g U_g^2}{\rho_l U_l^2} \tag{4}$$

where the subscripts g and l represent the gas and liquid properties, respectively, and ρ is the fluid density.

Finally, a Weber number for the flow can also be defined based on the mean slip velocity and the liquid nozzle exit diameter:

$$We = \frac{\rho_g \left(U_g - U_l\right)^2 d_l}{\sigma} \tag{5}$$

where σ is the surface tension of water.

All cases investigated in this work held the liquid flow rate constant at $Re_l = 1{,}100$ while the gas flow rate is varied such that $21{,}300 \leq Re_g \leq 180{,}000$, yielding $6 \leq M \leq 440$ and $39 \leq We \leq 2{,}900$. This corresponds to actual mean fluid velocities at the nozzle exit of $U_l = 0.48$ m/s and 34 m/s $\leq U_g \leq 290$ m/s.

2.3 X-ray Imaging

The high-speed flow visualization in this study was completed over four separate experimental campaigns at APS; this facility uses synchrotron technology to provide high brilliance X-ray beams that can be used for flow visualization (Kastengren et al., 2012; Kastengren and Powell, 2014). APS works by accelerating electrons to nearly the speed of light and then bending the path of the electrons. When the electron paths are bent by a bending magnet, wiggler, or undulator to change their direction, they emit an X-ray beam that is tangent to the direction of motion. The 7-BM beam line is used throughout this study, which provides high intensity white beam X-rays that can be used for 2D radiographic imaging with microsecond or sub-microsecond time resolution (Halls et al., 2017), and can produce very detailed 2D spatially and temporally resolved measurements of highly dynamic 3D events, like spray formation.

The setup for APS white beam radiography is shown in Fig. 2. A broadband X-ray beam is first emitted from the synchrotron ring. It then, optionally, passes through a set of filters to reduce soft X-rays and beam hardening, or to reduce the beam flux, if desired. The beam then passes through a rotating chopper wheel to further reduce the time-average power of the beam. The chopper wheel is composed of two 15.2 cm diam-
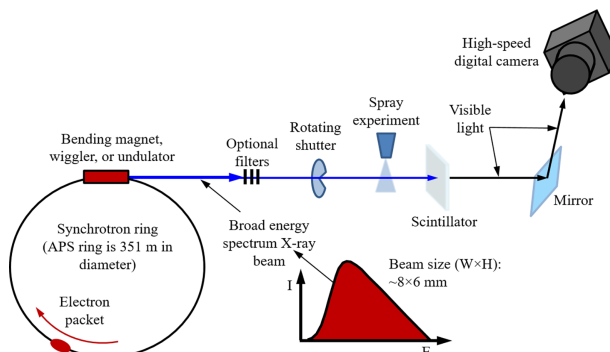
FIG. 2: Schematic of the advanced photon source (APS) experimental setup for high-speed white beam imaging (not to scale)

eter, 6.35 mm thick copper discs with two "pie wedge" openings cut into each disc. The discs are arranged such that a common open wedge of about 7.9° was used. The discs are spun at 0.5 Hz, yielding bursts of X-rays at 1 Hz. Although the chopper wheel was used to limit the average beam intensity, the acetal plastic nozzle still suffered radiation damage at the end of the last imaging campaign (Heindel et al., 2019).

After passing through the chopper wheel, the beam passes through the spray where the intensity of the beam decreases, depending on the amount of fluid through which it passes. The beam is then detected by a scintillator crystal. In this study, either a 500 μm thick YAG:Ce or a 100 μm thick LuAG scintillator crystal is used, depending on the test condition. Each scintillator crystal luminesces in the visible spectrum with an intensity proportional to the X-ray intensity. The visible light is then reflected by a mirror into a high-speed digital camera where an image is taken. The mirror is necessary because X-rays that are transmitted through the scintillator crystal could damage the camera if it is in the beam path. Additionally, shielding is placed around the imaging equipment to shield it from scattered X-rays that could damage the camera electronics.

In this study, one of two high-speed cameras are used. The first is a Photron FAST-CAM Mini AX50 with a frame rate of 2 kHz at full field of view (1024 × 1024 pixels). The second is a Photron FASTCAM SA-Z with a frame rate of 20 kHz at full field of view (1024 × 1024 pixels). In most cases, the cameras are operated using a reduce field of view to increase the frame rate. The cameras are connected to 105 mm–50 mm or 180 mm–50 mm macro-coupled lens combinations, respectively, to provide an effective magnification of 2.1× or 3.6×. At the highest SA-Z frame rates (100 kHz), a 1.4× teleconverter is also added to the lens combination to yield an effective magnification of 5.04×. Frame rates typically varied from 6 kHz for the slowest flow rates using the AX50 to 100 kHz for the highest flow rates using the SA-Z, with exposure times ranging from 1.05 μs to 3.75 μs, respectively.

Note the white beam in the 7-BM beam line at APS is not square (~ 8 mm wide by ~ 6 mm tall), and the intensity is most uniform in the beam center and then drops off toward the top and bottom edges. Furthermore, the spray is much larger than the

X-ray beam and most imaging is completed using a reduced field of view to utilize a higher camera frame rate and a more uniform beam flux. Hence, the beam center was the preferred imaging location. Additionally, to capture a wider spray region, a quasi-checkerboard imaging pattern is used to image several discrete locations. As illustrated in Fig. 3, a backlit image of the airblast nozzle spray shows a large spray extent while the white boxes show a quasi-checkerboard pattern used for white beam imaging of the same spray. The exact image size and checkerboard pattern depends on the specific camera, its image settings, and the area of interest within the spray. This study focuses on the near-field region and most white beam imaging is within 10 liquid needle diameters (about 2 gas nozzle diameters or 20 mm) or less from the nozzle exit. Furthermore, as the momentum flux ratio increased, the number of axial locations decreased because a full spray formed closer to the nozzle exit. Finally, the (x, y) coordinates of any given image represent the image center, where x is in the spray axial direction in mm, y is in the spanwise direction in mm, and (0, 0) represents the nozzle exit on the centerline of the liquid needle.

2.4 Image Normalization and Resolvable Object Size

Normalization of X-ray images helps to eliminates static bias which improves the image quality. Normalization is generally the first step in pre-processing the images for further analysis. Flat field normalization is used for this study and is defined by (Van Nieuwenhove et al., 2015):
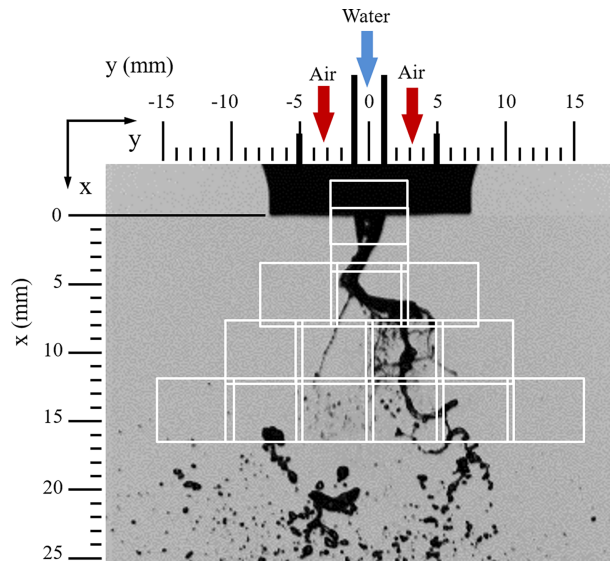
FIG. 3: Sample of overlapping image regions for white beam radiography (white boxes) overlaid on a backlit image of a representative spray with M = 6 and SR = 0 (units in mm).

$$N = \frac{(P - D)}{(F - D)} \qquad (6)$$

where P represents the original image, D is a dark field image, F is the flat field image, and N is the new normalized image. The mathematical operations in Eq. (6) are performed pixel-by-pixel. The dark field image is an image taken with no light entering the camera. The flat field image is created by taking a series of background images from a region where there is no spray or nozzle. In practice, sequences of background images (typically 400 frames) are acquired and averaged together to produce a flat field image with minimal noise. Additionally, as the cameras used in this study have a built-in calibration that does the dark field compensation onboard the camera, an ideal image of all zeros is used for the dark image.

From a visual inspection of the white beam images used in this study, the minimum resolvable object size is 5 pixels in diameter (20–25 μm, depending on camera and lens combination). Factors that affect the minimum resolvable object size include image resolution, contrast between the droplets and the background compared to the amount of noise that is present, and sources of error such as distortion and blurring which can be ignored in favor of the visual validation. The maximum resolvable object size is limited by the maximum size of droplet that can fit within the imaging frame.

3. RESULTS AND OBSERVATIONS

To show the advantages of X-ray imaging of sprays with respect to visible light imaging, Section 3.1 compares the visible features of a spray with M = 6 and SR = 1 between backlit imaging and X-ray white beam imaging. Section 3.2 makes overall comparisons of how the spray near-field changes as the momentum flux ratio is increased. Finally, the detailed features of spray breakup and changes in the liquid core are examined in Section 3.3.

3.1 Advantages of X-ray Imaging

Historically, backlit or shadowgraph imaging has been a popular method for studying the near-field region of a spray (Castrejón-García et al., 2011; Castrejón-Pita et al., 2013; Settles and Hargather, 2017; Dash et al., 2018). However, white beam X-ray radiography has recently gained traction because the technique provides information-rich images and enables rapid data collection. The high intensity of the X-ray beam makes it possible to have a short exposure so that fast-moving sprays can be captured without blur. The constant beam flux during image acquisition also allows images to be taken with high-speed cameras, and therefore the movement of the spray can be visualized (Li et al., 2017a). X-rays attenuate as they pass through liquid, so the resulting image can be correlated to the amount of liquid along the beam path (Li et al., 2019). Hence, the X-ray image is a 2D projection of the liquid content along the beam path, where the gray

scale variation correlates to liquid thickness, which provides information in the depth dimension. In contrast, backlit or shadowgraphy imaging uses visible light that reflects and refracts off of the gas–liquid interface and provides a binary image that shows where the projected liquid is, or is not, present, but provides no information on the amount of liquid in the image depth direction.

Figure 4 shows a comparison of a backlit image to white beam X-ray images for a spray with M = 6 and SR = 1. It is important to note that backlit imaging can easily cover a larger spray area than synchrotron-based white beam imaging, but tube source X-rays can be used to capture large spray regions if there is a sufficient signal-to-noise ratio in the images (Heindel, 2018; Li et al., 2019). The major difference between backlit and white beam imaging, which is important for analysis, is the level of detail that is available. Backlit imaging can provide a long imaging sequence and intact length and spray angle can be easily determined from the images (Bothell et al., 2020a, 2020b; Morgan and Heindel, 2021). However, the resulting images only show the presence of liquid (a shadow), and liquid thickness cannot be determined. Additionally, if multiple fluid structures like overlapping droplets exist along the light path, they appear as a single object in the recorded backlit image. In contrast, for X-ray images like those shown in Fig. 4, the thicker liquid corresponds to the darker region. The gray-scale level can be correlated to the optical depth of the liquid region
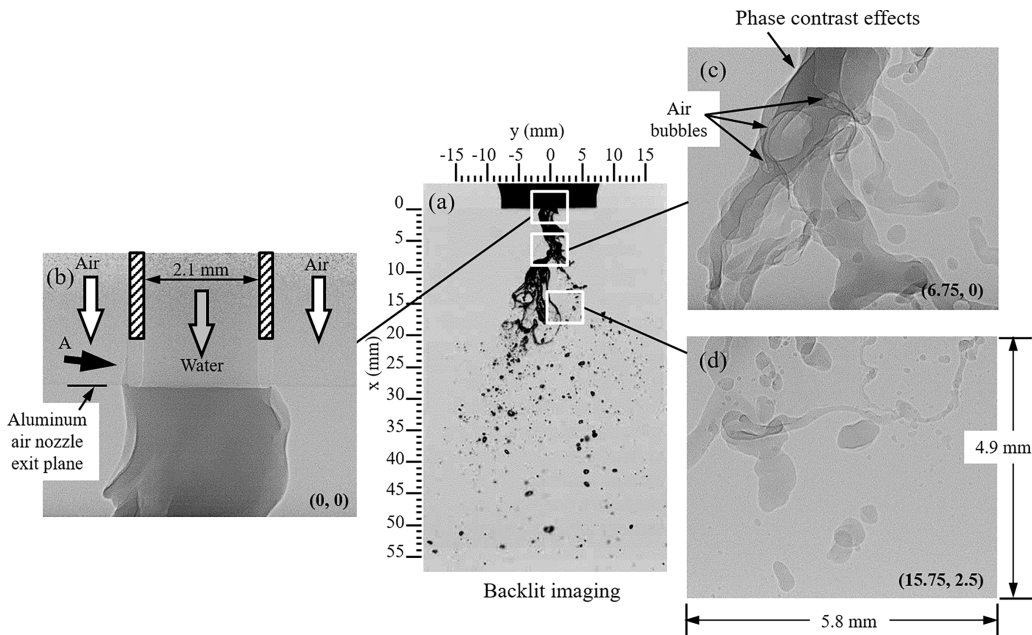
FIG. 4: Co-axial spray with M = 6 and SR = 1. (a) Backlit image of large spray region. (b) White beam X-ray image at the nozzle exit, (0, 0). (c) White beam X-ray image downstream of the nozzle exit, (6.75, 0). (d) White beam X-ray image further downstream, (15.75, 2.5). All coordinate locations correspond to the (x, y) image center and are given in mm.

(Li et al., 2019), so the darker the region, the more liquid is present between the X-ray source and detector. This also allows the ability to identify overlapping flow structures. The benefits of white beam X-ray images over backlit images are very apparent at the nozzle exit, as shown in Fig. 4b. In this region, X-rays allow imaging inside the outer aluminum air nozzle. The liquid needle walls are also identified. There is also clear evidence of liquid wicking up the outside of the water needle (see the large arrow marked with "A" in Fig. 4b), which is impossible to capture with backlit imaging. Further downstream, air bubbles within the liquid region and overlapping liquid structures are also visible (Fig. 4c and 4d, respectively). The enhanced white regions at the air-water interface are also visible in the X-ray images and are due to phase contrast effects (Heindel, 2018).

3.2 Overall Spray Observations and Comparisons

Figure 5 shows various white beam images at selected spray locations for three different momentum flux ratios. Since the images are acquired in a checkerboard fashion (see Fig. 3), they are uncorrelated. For each flow condition, the image size may also differ and is a function of the camera and frame rate, but the physical scale is consistent across all images to show the trade-offs between frame rate and image size. Note the images presented in Fig. 5 (and all subsequent images) represent a typical image from the respective region, and all described observations represent a compilation of observations after viewing several hundred to several thousand images for each flow condition and location. Finally, the liquid flow rate is held constant at $Re_l = 1,100$ for each condition, $SR = 0$, and the gas flow rate is increased to increase the momentum flux ratio.

The top image for all momentum flux ratios shows the approximate location of the liquid needle exit as the dark vertical lines, and the edge of the copper grounding ring from the acetal plastic nozzle is visible at the very top of the image. Focusing initially on the $M = 6$ images, bag formation is easily captured as the water and air exit the nozzle. The bags breakup into ligaments as they progress downstream, which breakup into droplets. Increasing the gas flow rate such that the momentum flux ratio increased by a factor of 5 ($M = 30$) and then by another factor of 5 ($M = 150$), shows that the extent of the intact liquid region downstream of the nozzle exit gets shorter as the momentum flux ratio increases. Additionally, the flow structures that are observed downstream get smaller and more dispersed. More details on these structures are provided below.

## 3.3 Qualitative Description of Spray Breakup

The following is a detailed qualitative description of spray breakup for sprays with various momentum flux ratios. Spray dynamic descriptors follow common identifiers, when available. If a name does not exist for a particular dynamic, then identifiers are chosen to best represent the given dynamic structure.
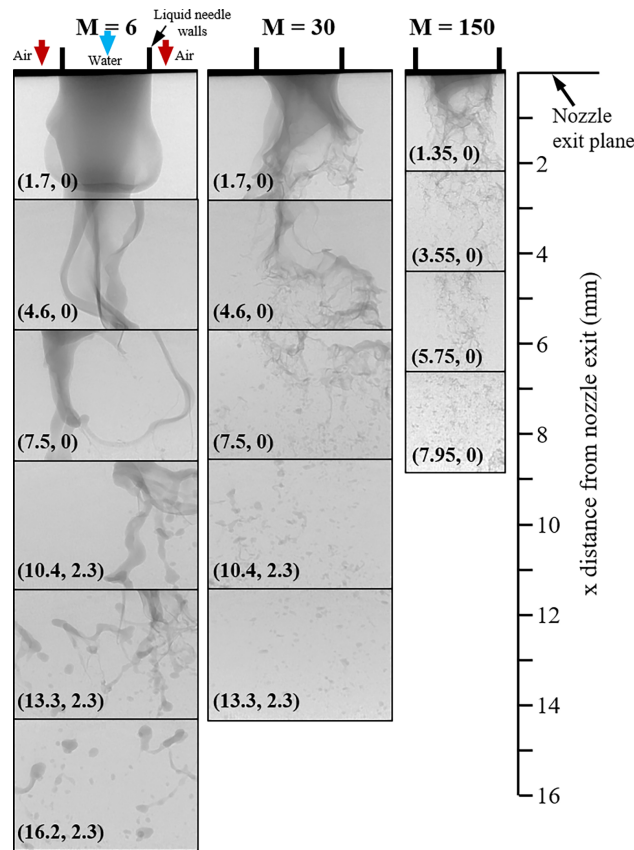
FIG. 5: White beam X-ray images of an airblast atomizer showing how the spray changes in response to increasing the momentum flux ratio and downstream distance. Coordinate locations correspond to the (x, y) image center and are given in mm. Note lower images are slightly off-center.

3.3.1 Airblast Atomizer with M = 6

When $M = 6$ and $SR = 0$, a slowly oscillating liquid stream is observed right at the liquid nozzle exit. Some of the water wicks up the outside of the liquid nozzle (Heindel, 2018); X-rays allow for this observation because they penetrate the opaque nozzle. As the spray progresses downstream, instabilities form along the gas–liquid interface where the gas tries to penetrate the liquid, forming bags as shown in Fig. 5 at $M = 6$. The bag grows and deforms the liquid jet leading to ligament formation, shown in Fig. 6a as structures identified as "A." As the bag thins, ligaments form that are connected by a thinning liquid sheet. As the liquid moves further downstream, the liquid sheet continues to thin and eventually ruptures, shown in Fig. 6a as structures identified as "B." Figure 6b has been enlarged to emphasize the edge of a liquid sheet ("B") right before rupture. When bag breakup occurs, ligaments and many small droplets (with respect to the size of the
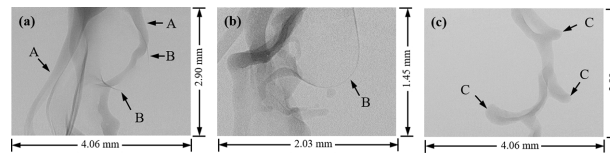
FIG. 6: Selected spray structures observed with white beam X-ray imaging from an airblast atomizer with M = 6 and SR = 0. (a) Initial ligament formation; (b) bags, ligaments, and thin liquid sheets (note the image size has been increased for emphasis); (c) secondary bag and ligament formation.

ligaments) form. The thinnest portion of the bag produces the smallest droplets, whereas the thicker edge of the bag generates the ligaments and larger droplets.

The liquid ligaments eventually separate from the main liquid stream at a distance known as the intact length (where the continuous liquid region is no longer observed). The intact length is not a constant value, but has sharp oscillations where a ligament may form at the tip and then abruptly break off. Because white beam imaging of the spray is completed in sections, and the intact length may span more than one image region, it is challenging to provide a precise measure with the imaging technique employed here. A comparison of intact length measures with different techniques has been completed for the sprays shown here (Bothell et al., 2020a).

As ligaments continue downstream, they can be stretched by the high-speed air surrounding them, increasing the ligament speed with downstream distance. This also leads to secondary bag and ligament formation, as shown in Fig. 6c with the structures identified as "C;" these structures continually stretch, become thinner, and eventually breakup into smaller droplets.

The separated ligaments stretch as they move downstream, but the process is not uniform. For example, Fig. 7 shows an image sequence of ligament stretching and breakup, where the time between frames is 555 µs (several frames are omitted between each image). Bulges in the ligament "A" are connected by thin liquid regions. The bulges grow and the connecting regions thin and eventually rupture, as shown by "B" and "C," where the bulges form droplets, identified by "D." The breakup process forms nonuniform droplets as well as many satellite droplets, as shown by the enhanced image region and objects identified as "E."
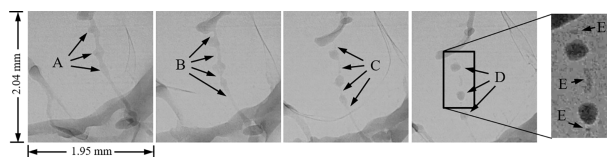

FIG. 7: Ligament breakup at M = 6 with time between frames of 555 µs. Structures identified as bulges (A), thin liquid regions connecting the bulges (B and C), thin regions rupture forming droplets (D) and satellite droplets (E).

The motion of the ligaments is quite dynamic, with different parts of the ligament moving at different velocities. They can stretch axially, collapse axially to form mushroom-shaped structures (Fig. 8a), or tumble. Horizontal ligaments generally stretch more in the middle to create a U-shape and then break apart. These structures may rupture further along different paths, depending on if they are large or small. The larger mushroom structures often split into secondary ligaments, or the upper and lower portions separate into two droplets. Smaller mushroom structures often form a bag before breaking into smaller droplets.

A unique phenomenon that is visible using X-ray imaging, but not shadowgraphy or backlit imaging, is air bubbles trapped inside liquid regions. When bubbles form because of bags folding on the edge of the liquid stream, they move significantly slower than the rest of the liquid, and some have been observed to migrate upwards towards the nozzle exit. Larger bubbles may disappear as the liquid separates into ligaments and droplets. Smaller bubbles often get trapped inside the liquid and move with it. Examples of air bubbles inside the liquid are highlighted in Fig. 8, where they are found in the observed mushroom structure, inside a liquid ligament, and inside individual droplets. Bubbles trapped inside liquid droplets could have a significant effect on the combustion process if the spray was a fuel injector. Bubbles could also create hollow metal powders from liquid metal sprays that could be detrimental to additive manufacturing processes (Anderson et al., 2018).

In addition to breakup, the liquid structures (ligaments, bags, mushrooms, liquid sheets, and droplets) sometimes collide with each other. During collisions, the masses often combine; they either remain as a single droplet or may undergo secondary breakup downstream. A series of images showing droplet collision is provided in Fig. 9, where several image frames are omitted from this sequence to provide a representation of the collision process.

Similar spray structures continued to form and breakup throughout the near-field region until the spray is broken into many droplets. Once the spray is composed of only droplets, the droplet size distribution begins to stabilize. Secondary atomization, with droplets breaking apart into smaller droplets, may still occur, but at a slower rate than primary atomization. Droplets that are most likely to break up during secondary atomization are typically larger and the breakup is caused by instabilities that form on the droplet surface. When secondary breakup occurs, the droplets first deform into
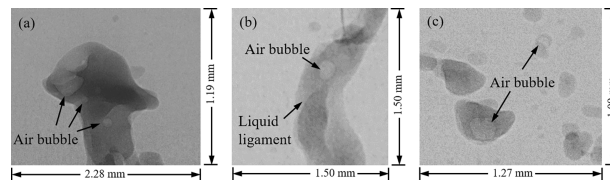
FIG. 8: Sample spray structures recorded with white beam X-ray imaging with M = 6: (a) a mushroom-like structure, (b) an air bubble inside a liquid ligament, (c) air bubbles inside liquid droplets. Note the image size varies to emphasize the given structure.
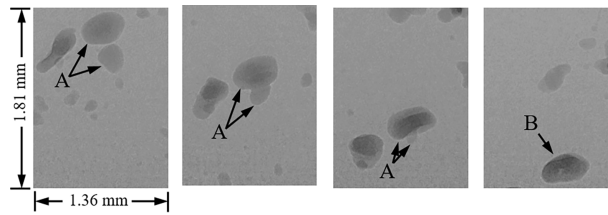
FIG. 9: Droplet collision at M = 6 with time between frames of 1.1 ms. The two original droplets (A) and the coalesced droplet (B).

a thin oblong shape. The center region of the oblong shape narrows as the ends are pulled apart. Once the center of the oblong shape becomes thin enough, the droplet will suddenly break apart into two droplets, usually of similar size. The droplets move with approximately the same downstream velocity but continue moving further away from each other after breakup. One or more satellite droplets may also form between the larger separated droplets, where the satellite droplets are much smaller than the two main droplets. A typical example of this process is shown in Fig. 10, where the secondary breakup of two droplets are observed simultaneously. Note the time between each image is 1.1 ms.

3.3.2 Airblast Atomizer with M = 30

Many of the phenomena that are observed from the airblast atomizer at M = 6 are also captured when M = 30, but the liquid breakup occurs much faster and closer to the nozzle exit, which results in smaller downstream droplets. With a more active spray region, some of the breakup mechanics are too fast to capture in sequence unless the frame rate is greater than 45 kHz. The higher momentum flux ratio also results in more interference with overlapping spray dynamics.

When the momentum flux ratio increases to M = 30 and SR = 0, wicking around the nozzle is not visible from white beam X-ray radiographs as it was with M = 6. Necking occurs in the attached liquid portion of the spray very near the liquid nozzle exit, identified as "A" in Fig. 11a with the narrowest point 0.5–1.0 d_l downstream of the exit plane.
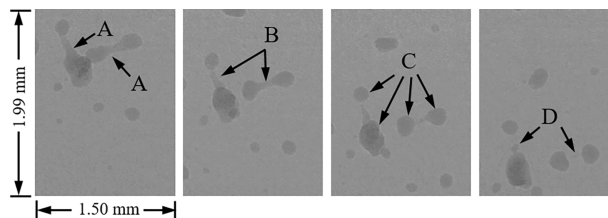
FIG. 10: Secondary droplet breakup with M = 6. Oblong structures (A) are first elongated and stretched (B). The elongated droplets break and form secondary droplets (C) and satellite droplets (D).
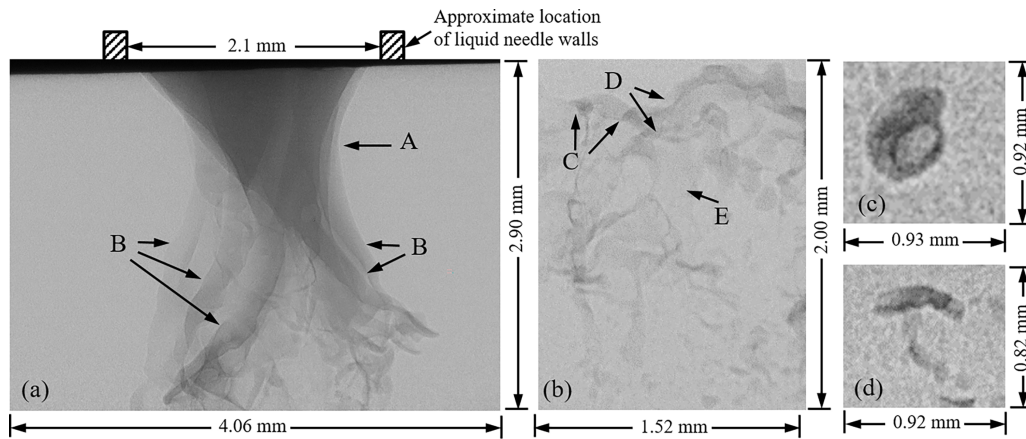
FIG. 11: Spray formations seen in white beam X-ray images from a coaxial spray with M = 30 and SR = 0. (a) Liquid necking (A) and ligament formation (B); (b) liquid web structure containing liquid ligaments (C), ligament bulges and necking (D), and liquid sheets connecting the ligaments (E); (c) bubble in a liquid droplet; and (d) mushroom-like structure.

Ligament formation and eventual separation is observed after the narrowing liquid region, identified as "B" in Fig. 11a. The separation and breakup of ligaments is rapid in comparison to a spray with M = 6, and a larger number of liquid sheets and bags are present in the spray region just below the liquid necking.

In sequential images in regions like that of Fig. 11a, the majority of the mass appears to oscillate back and forth across the 2D image projection. It is hypothesized that the oscillation is more of a 3D helical flow with the direction varying in a chaotic manner. Stereographic imaging is needed to confirm this. However, manual tracking of the liquid motion shows that the motion did not follow a sinusoidal pattern. In comparison to the spray with M = 6, a spray with M = 30 has ligaments that are much narrower, but still create liquid sheets between the ligaments before they quickly break apart. With the increased shear forces from the higher gas flow rate, the ligaments become very thin so that when they do break, much smaller droplets are observed compared to those at M = 6.

At the higher gas flow rate, liquid sheets form at a high rate where some rejoin with liquid ligaments and others become bags that break apart into small droplets. The droplets that form from the bag rim are larger than those that form from the bag, but they are still smaller than those observed at M = 6. After initial ligament formation, the liquid structures transition from individual ligaments to ensembles that appear web-like, as shown in Fig. 11b. The webs contain ligaments, identified as "C" and ligaments with bulges and necking, identified as "D." Many of the ligaments are connected by liquid sheets, identified as "E." These web-like structures are highly dynamic, and as they travel downstream they start to breakup. Breakup begins with the thin liquid sheet regions, which create the smallest droplets, and then progress to ligament breakup. This process continues until the spray is composed entirely of droplets. Some of the droplets

contain bubbles (Fig. 11c), and some form mushroom-like structures (Fig. 11d). In both cases, these structures are smaller than those observed with M = 6.

Figure 12 provides a series of images separated by 278 μs showing the expansion and breakup of a web-like structure. Note the primary shapes in each image change from frame-to-frame due to the shear forces imparted on the liquid from the gas stream. Many of the larger structures in Fig. 12 elongate and undergo secondary breakup. When secondary breakup occurs at M = 30, the process starts in a similar fashion to that observed with M = 6, where droplets first deform into a thin oblong shape. The center region of the oblong shape then narrows as the edges pull apart. It is common to see the oblong shape get stretched into a thin ligament and break into multiple droplets if enough liquid mass is present. It is also common to see a small bag form near the center of the oblong shape, which abruptly disappears upon secondary breakup. A series of images, separated by 278 μs, showing an oblong object forming a bag and then breaking up is shown in Fig. 13. Note, this bag formation process is similar to that observed with M = 6, but the bags and resulting droplets are much smaller at the higher gas flow rate with M = 30.

The majority of the liquid spray mass continues to sweep across the spray field even when the spray is all droplets. Backlit visible light imaging at this condition shows that
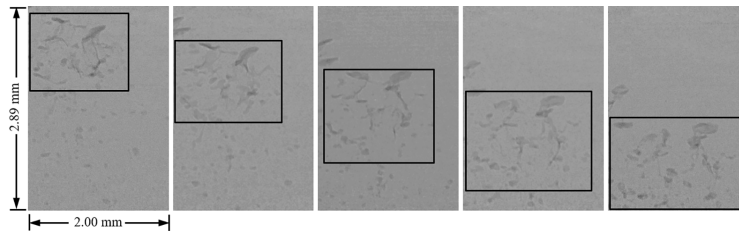
FIG. 12: Downstream spray web-like structures observed with white beam X-ray imaging and M = 30. Each image is separated by 278 μs. The black box tracks a web-like structure as it moves through the spray field, expanding and breaking apart.
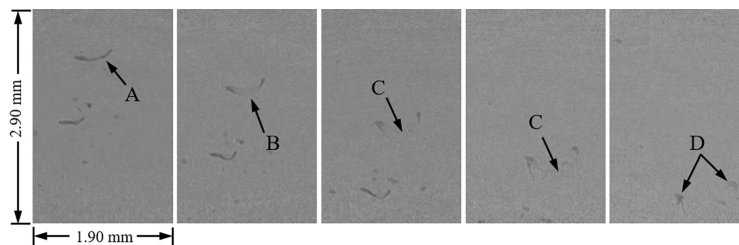
FIG. 13: Secondary breakup at M = 30. Each image is separated by 278 μs. Stretching of the initial droplet into an oblong shape (A), which then undergoes bag formation (B) and breakup (C), that leads to two resulting droplets (D).

this sweeping motion is due to the upstream oscillatory motion, where the liquid continues to move in the direction that is observed upstream.

3.3.3 Airblast Atomizer with M > 30

The spray dynamics are similar when $30 \leq M \leq 66$, but change considerably when M = 95 ($66 < M < 95$ were not visualized). Most of the formation phenomena occur very near the nozzle exit. Figure 14 shows sample images at the nozzle exit for various gas flow rates while SR = 0. All of these images were acquired with the SA-Z camera and the specific camera frame rates and image sizes are summarized in Table 1. Note that the physical scale of each image is identical. The image (x, y) coordinate that identifies the image center relative to the liquid needle exit is also provided. Additionally, videos for each of these conditions can be found in the supplemental material.

Recall that the liquid needle has an ID of $d_l = 2.1$ mm ID and an OD of $D_l = 2.7$ mm; this is represented in Fig. 14 with the black bars on top of each image. When M = 6, the liquid intact length extends beyond the image region. Bags also continuously form and extend beyond the image region. The liquid has been observed to wick up the outer diameter of the liquid needle so as it exits nozzle, the intact liquid core extends spanwise beyond the inner wall. This has also been shown numerically if the wetting dynamics are properly modeled (Vu et al., 2021).

Increasing the momentum flux ratio to M = 30 causes the liquid region to narrow as it exits the liquid needle and appear to oscillate in this 2D projection. Bags that do form for this flow condition are short-lived and breakup into ligaments that appear to be pulled from the liquid region. Air bubbles are also observed to form in the liquid region of the image, and some are transported into the next image region while others disappear as they pop.

Similar dynamics are observed when M = 48 and M = 66. The main difference is the intact length decreases with increasing M. When M = 95, the flow structure appears to form an upside-down crown, where the inside of the crown is a depressed region of low liquid content. It is hypothesized that as high velocity gas exits the nozzle around the periphery of the slower liquid region, a toroidal recirculation cell forms with high velocity gas pushing the liquid upstream in the center of the liquid needle. This results in liquid being pulled from the outer region and a liquid depression forms in the inner region, creating the crown. Machicoane et al. (2019) have shown that when swirl is added to this flow, the crown formation occurs at lower momentum flux ratios.

Increasing the momentum flux ratio to M = 150 reveals the crown walls periodically get very short such that a portion may disappear. Using the aluminum outer air nozzle, Machicoane et al. (2019) showed that when this happens, the crown partially dewets from a portion of the liquid needle exit, and this process is very dynamic; they called this flow "unstable crown." Air bubbles also periodically form in the inner region of the crown and then dissipate.

Further increasing the gas flow rate to M = 210 shortens the crown region and it still remains unstable. Some of the liquid ligaments that are pulled from the crown edges are
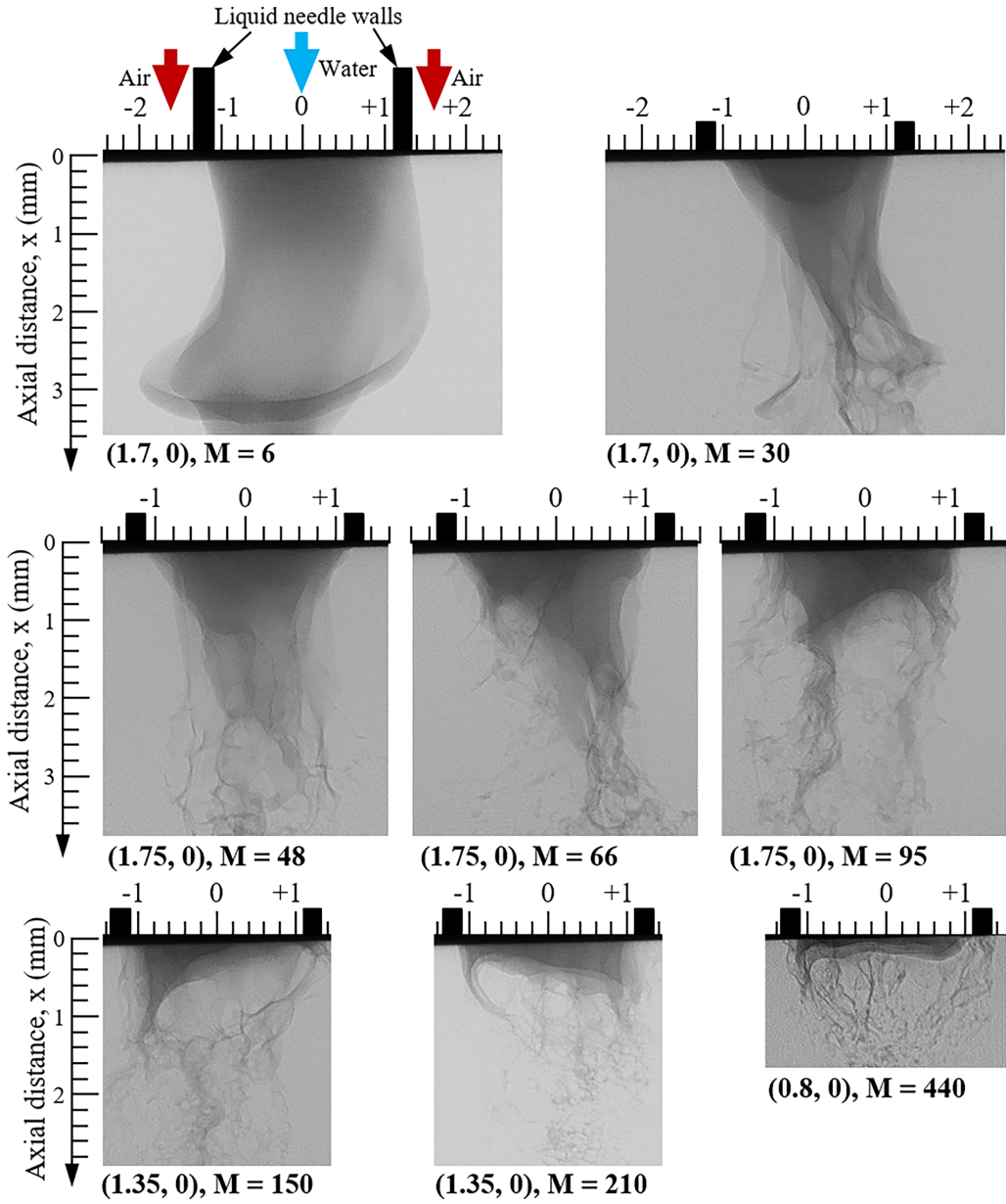
FIG. 14: White beam X-ray images right at the nozzle exit for various momentum flux ratios, while SR = 0 and the liquid flow rate is fixed at Re_l = 1,100. Specific flow conditions are summarized in Table 1. Coordinate locations correspond to the (x, y) image center and are given in mm, which also represents the scale in each image.

TABLE 1: Gas flow rates and camera settings for the nozzle exit images shown in Fig. 14. The liquid flow rate was fixed for all conditions at $Re_l = 1,100$ ($Q_l = 0.099$ LPM) and SR = 0

Q_g (SLPM)	Re_g	M	Frame rate (kHz)	Frame size, H × V (pixels)	Frame size, H × V (mm)
150	21,300	6	36	896 × 640	4.82 × 3.56
330	46,700	30	36	896 × 640	4.82 × 3.56
420	59,600	48	45	640 × 664	3.56 × 3.69
490	69,600	66	45	640 × 664	3.56 × 3.69
590	83,800	95	45	640 × 664	3.56 × 3.69
730	104,000	150	67.2	512 × 520	2.84 × 2.89
870	124,000	210	67.2	512 × 520	2.84 × 2.89
1270	180,000	440	60	768 × 424	3.05 × 1.68

caught in the recirculation cells and wrap upstream as they dissipate. Air bubbles also appear to migrate upstream in the liquid flow. At the highest momentum flux ratio of M = 440, the crown is very short and still unstable. One interesting observation at this momentum flux ratio is that some of the small liquid droplets that do form migrate upstream of the flow direction in the nozzle center. We believe this happens in the center region of the liquid needle and not outside the liquid needle because the high velocity gas stream outside the liquid region would prevent liquid backflow. This confirms the presence of a toroidal recirculation cell where high velocity gas is pushing the liquid in the center of the flow in the opposite direction.

The upstream migration of air bubbles and liquid droplets is further confirmed in Fig. 15, where images taken at 100 kHz are shown right at the nozzle exit for M = 210 and M = 440 with SR = 0. Note that for this image acquisition speed, the image size, which is shown on the figure, is reduced to a region smaller than the liquid needle ID and each image is centered on the liquid needle centerline. Each image in the shown sequence is separated by 50 μs (every 5th image at a frame rate of 100 kHz). When M = 210, the air bubble caught in the interior of the liquid crown migrates upstream over the 200 μs time frame, as shown by the white circled region. When M = 440, a liquid droplet is identified in the white circled region and it also migrates upstream over the given time period. It is unlikely that observations such as those shown in Figs. 14 and 15 could be made with backlit or shadowgraph imaging.

4. FUTURE APPLICATIONS AND CHALLENGES

High-speed white beam imaging is a powerful flow visualization technique that can be used to capture high-speed multiphase flows that are obscured when using visible light or lasers. The current work shows qualitative observations. Quantitative measures of equivalent path length (EPL), defined as the accumulated liquid along the beam path, are easily acquired using focused beam measurements (Li et al., 2019; Bothell et al.,
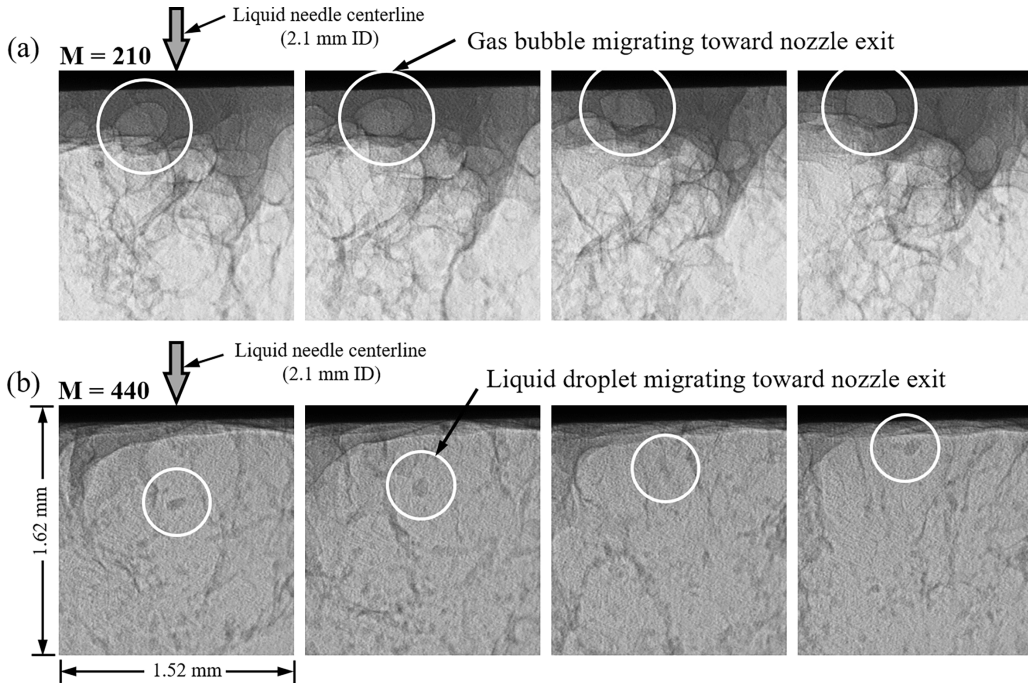
FIG. 15: Close-up images taken at 100 kHz right at the exit of the liquid needle for (a) M = 210 showing the upstream migration of an air bubble, and (b) M = 440 showing the upstream migration of a liquid droplet. The time between frames for each sequence is 50 μs.

2020a; Kastengren et al., 2014). In this imaging mode, Beer-Lambert's Law can be used to determine EPL:

$$\text{EPL} = \ell = \frac{1}{\mu} \ln \left[\frac{I_0}{I(t)} \right] \tag{7}$$

where μ is the attenuation coefficient. In white beam imaging, however, μ is not known precisely because it is a function of X-ray wavelength, and white beam imaging has a variety of wavelengths, which are differentially attenuated, depending on the material and material thickness. This complicates the analysis, but with proper calibration and X-ray energy modeling, the white beam-determined EPL may be approximated; this is the focus of some of our future efforts.

Additionally, quantitative image analysis to determine droplet size and velocity will be completed in the future. Challenges remain, however, in that multiple droplets imaged with X-rays can be easily tracked with the human eye, even when they overlap for a period of time. Developing imaging analysis tracking software that reliably captures these droplets is more complicated due to overlapping structures and small variations in X-ray image contrast.

Another challenge is that the X-ray beam from the APS synchrotron facility is limited in size, so the maximum field of view is only ~ 8 mm wide by ~ 6 mm tall. Additionally, the beam flux near the edges of the beam are not as uniform or steady as near the center, and these fluctuations will create X-ray image contrast variations with time and location.

Finally, the X-ray beams generated at APS are fixed in space and correspond to tangents of the synchrotron ring. Hence, X-ray flow visualization from multiple projections at the same instant in time, like those from two or more tube X-ray sources (Heindel et al., 2008; Mudde, 2010; Halls et al., 2019), is extremely challenging. One group has attempted this (Hoshino et al., 2011), but their synchrotron beam width was very large (~ 300 mm), and only two projections were acquired simultaneously with an angle between the projections of only about 15°.

One possible method to do computed tomography of sprays using white beam imaging is to mount the spray on a rotation system, and then rotate the spray to produce the multiple views required for tomographic reconstruction. If the spray is periodic like a liquid fuel injector, it is possible to phase-lock the measurements to produce time-resolved 3D images, assuming the injection process is highly repeatable (Tekawade et al., 2020). Additionally, to view multiple spray locations for larger sprays like the one used in this study, the spray has to be mounted on an x-y translation stage. The desire to look at pressurized spray systems requires a small pressurized spray facility where the entire system can be mounted on an x-y translation stage (Kastengren et al., 2009), or the entire spray nozzle and x-y translation stage has to be mounted within a pressured facility (Burtnett et al., 2021).

5. CONCLUSIONS

This observational study showed that high-speed white beam X-ray imaging, using the Advanced Photon Source at Argonne National Laboratory, provided unique advantages over traditional optical high-speed imaging techniques such as backlit imaging. The increased detail and high temporal and spatial resolution enabled a very detailed qualitative analysis of the spray structure, dynamics, and breakup. Using a canonical airblast atomizer, overlapping bags, ligaments, and bubbles were clearly observed with X-ray imaging. As the momentum flux ratio increased with a constant liquid flow rate, the atomization process moved toward the nozzle exit. Bag and ligament formation still occurred, but at a faster rate. When $M \geq 95$, an unstable crown formed at the liquid needle exit, and as the momentum flux ratio increased, the crown became shorter and more dynamic.

One unique advantage of high-speed white beam X-ray imaging is that overlapping flow structures can be captured including ligaments, droplets, mushrooms, and webs. Furthermore, air bubbles within liquid regions were clearly captured. This also allowed for the observation that air bubbles and liquid droplets migrated upstream within the liquid crown at the highest momentum flux ratios on this study. These structures are not observed with optical imaging techniques.

One challenge with high-speed white beam X-ray imaging is the limited field of view. To capture the entire spray region, particularly at the lower momentum flux ratios, several overlapping imaging regions were required, and some of the flow structures could not be tracked from region to region.

ACKNOWLEDGMENTS

REFERENCES

Aliseda, A. and Heindel, T.J., X-ray Flow Visualization in Multiphase Flows, *Ann. Rev. Fluid Mechan.*, vol. **53**, pp. 543–567, 2021.

Anderson, I.E., White, E.M.H., and Dehoff, R., Feedstock Powder Processing Research Needs for Additive Manufacturing Development, *Curr. Opin. Solid State Mat. Sci.*, vol. **22**, no. 1, pp. 8–15, 2018.

Bachalo, W., Spray Diagnostics for the Twenty-First Century, *Atom. Sprays*, vol. **10**, no. 3–5, pp. 439–474, 2000.

Bothell, J.K., Machicoane, N., Li, D., Morgan, T.B., Aliseda, A., Kastengren, A.L., and Heindel, T.J., Comparison of X-ray and Optical Measurements in the Near-Field of an Optically Dense Coaxial Air-Assisted Atomizer, *Int. J. Multiphase Flow*, vol. **125**, p. 103219, 2020a.

Bothell, J.K., Morgan, T.B., and Heindel, T.J. Image-Based Feedback Control for a Coaxial Spray, *J. Fluids Engin.*, vol. **142**, no. 11, p. 114501, 2020b.

Burtnett, T.B., Morgan, T.B., Dahlstrom, T.C., Aliseda, A., and Heindel, T.J., A Pressurized Tank for High Flow Rate Atomization Studies, *ICLASS 2021, 15th Tri. Int. Conf. Liq. Atom. Spray Syst.*, Edinburgh, UK, August 29–September 2, 2021.

Cartz, L., *Nondestructive Testing*, Materials Park, OH: ASM International, 1995.

Castrejón-García, R., Castrejón-Pita, J., Martin, G., and Hutchings, I., The Shadowgraph Imaging Technique and Its Modern Application to Fluid Jets and Drops, *Revista Mex. Física*, vol. **57**, no. 3, pp. 266–275, 2011.

Castrejón-Pita, J.R., Castrejón-García, R., and Hutchings, I.M., High Speed Shadowgraphy for the Study of Liquid Drops, in *Fluid Dynamics in Physics, Engineering and Environmental Applications*, J. Klapp, A. Medina, A. Cros and C.A. Vargas, Eds., Berlin: Springer, pp. 121–137, 2013.

Coletti, F., Benson, M.J., Sagues, A.L., Miller, B.H., Fahrig, R., and Eaton, J.K., Three-Dimensional Mass Fraction Distribution of a Spray Measured by X-ray Computed Tomography, *J. Engin. Gas Turbines Power*, vol. **136**, no. 5, pp. 1–8, 2014.

Dash, A., Jahangir, S., and Poelma, C., Direct Comparison of Shadowgraphy and X-ray Imaging for Void Fraction Determination, *Meas. Sci. Technol.*, vol. **29**, no. 12, p. 125303, 2018.

Fansler, T.D. and Parrish, S.E., Spray Measurement Technology: A Review, *Meas. Sci. Technol.*, vol. **26**, no. 1, pp. 1–34, 2015.

Halls, B.R., Heindel, T.J., Kastengren, A.L., and Meyer, T.R., Evaluation of X-ray Sources for Quantitative Two- and Three-Dimensional Imaging of Liquid Mass Distribution in Atomizing Sprays, *Int. J. Multi-phase Flow*, vol. **59**, pp. 113–120, 2014.

Halls, B.R., Radke, C.D., Reuter, B.J., Kastengren, A.L., Gord, J.R., and Meyer, T.R., High-Speed, Two-Dimensional Synchrotron White-Beam X-ray Radiography of Spray Breakup and Atomization, *Optics Express*, vol. **25**, no. 2, pp. 1605–1617, 2017.

Halls, B.R., Rahman, N., Slipchenko, M.N., James, J.W., McMaster, A., Ligthfoot, M.D.A., Gord, J.R., and Meyer, T.R., 4D Spatiotemporal Evolution of Liquid Spray Using Kilohertz-Rate X-ray Computed Tomography, *Optics Lett.*, vol. **44**, no. 20, pp. 5013–5016, 2019.

Hampel, U., Image Reconstruction for Hard Field Tomography, in *Industrial Tomography: Systems and Applications*, M. Wang, Ed., Waltham, MA: Elsevier, pp. 347–376, 2015.

Heindel, T.J., A Review of X-ray Flow Visualization with Applications to Multiphase Flows, *ASME J. Fluids Engin.*, vol. **133**, no. 7, p. 074001, 2011.

Heindel, T.J., X-ray Imaging Techniques to Quantify Spray Characteristics in the Near-Field, *Atom. Sprays*, vol. **28**, no. 11, pp. 1029–1059, 2018.

Heindel, T.J., Gray, J.N., and Jensen, T.C., An X-ray System for Visualizing Fluid Flows, *Flow Meas. Instrum.*, vol. **19**, no. 2, pp. 67–78, 2008.

Heindel, T.J., Morgan, T.B., Burtnett, T.J., Bothell, J.K., Li, D., Aliseda, A., and Machicoane, N., High-Speed Flow Visualization of a Canonical Airblast Atomizer Using Synchrotron X-rays, *AJK2019– Joint ASME/JSME/KSME Fluids Engin. Div. Summer Meeting*, San Francisco, CA, July 28–August 1, ASME Press, Paper Number: AJKFLUIDS2019-4992, 2019.

Hoshino, M., Uesugi, K., Pearson, J., Sonobe, T., Shirai, M., and Yagi, N., Development of an X-ray Real-Time Stereo Imaging Technique Using Synchrotron Radiation, *J. Synchrotron Radiat.*, vol. **18**, no. 4, pp. 569–574, 2011.

Hsieh, J., *Computed Tomography: Principles, Design, Artifacts, and Recent Advances*, Bellingham, WA: SPIE Press, 2003.

Huck, P.D., Machicoane, N., Osuna-Orozcon, R., and Aliseda, A., Experimental Characterization of a Canonical Two-Fluid Coaxial Atomizer, *ICLASS 2018, 14th Tri. Int. Conf. Liquid Atom. Spray Syst.*, Chicago, IL, July 22–26, 2018.

Karathanassis, I.K., Heidari-Koochi, M., Zhang, Q., Hwang, J., Koukouvinis, P., Wang, J., and Gavaises, M., X-ray Phase Contrast and Absorption Imaging for the Quantification of Transient Cavitation in High-Speed Nozzle Flows, *Physics Fluids*, vol. **33**, no. 3, p. 032102, 2021.

Kastengren, A.L. and Powell, C., Synchrotron X-ray Techniques for Fluid Dynamics, *Exper. Fluids*, vol. **55**, no. 3, pp. 1–15, 2014.

Kastengren, A.L., Powell, C.F., Arms, D., Dufresne, E.M., Gibson, H., and Wang, J., The 7BM Beamline at the APS: A Facility for Time-Resolved Fluid Dynamics Measurements, *J. Synchrotron Radiat.*, vol. **19**, no. 4, pp. 654–657, 2012.

Kastengren, A.L., Powell, C.F., Wang, Y., Im, K.-S., and Wang, J., X-ray Radiography Measurements of Diesel Spray Structure at Engine-Like Ambient Density, *Atom. Sprays*, vol. **19**, no. 11, pp. 1031–1044, 2009.

Kastengren, A.L., Tilocco, F.Z., Duke, D.J., Powell, C.F., Zhang, X., and Moon, S., Time-Resolved X-ray Radiography of Sprays from Engine Combustion Network Spray a Diesel Injectors, *Atom. Sprays*, vol. **24**, no. 3, pp. 251–272, 2014.

Khlifa, I., Vabre, A., Hočevar, M., Fezzaa, K., Fuzier, S., Roussette, O., and Coutier-Delgosha, O., Fast X-ray Imaging of Cavitating Flows, *Exper. Fluids*, vol. **58**, no. 11, p. 157, 2017.

Li, D., Bothell, J.K., Morgan, T.B., Heindel, T.J., Aliseda, A., Machicoane, N., and Kastengren, A.L., High-Speed X-ray Imaging of an Airblast Atomizer at the Nozzle Exit, *2017 APS-DFD Meeting*, Denver, CO, November 19–21, 2017, APS-DFD Gallery of Fluid Motion Video Entry #V0026, 2017a.

Li, D., Morgan, T.B., Pulfer, L.D., and Heindel, T.J., Measurement of near-Field Spray Characteristics with Broadband X-rays, *ASME 2017 FEDSM - Fluids Division Summer Meeting*, Hilton Waikoloa Village, Waikoloa, Hawaii, July 30–August 3, ASME Press, Paper Number FEDSM2017-69088, 2017b.

Li, D., Bothell, J.K., Morgan, T.B., Machicoane, N., Aliseda, A., Kastengren, A.L., and Heindel, T.J., Time-Averaged Spray Analysis in the Near-Field Region Using Broadband and Narrowband X-ray Measurements, *Atom. Sprays*, vol. **29**, no. 4, pp. 331–349, 2019.

Lightfoot, M.D., Schumaker, S.A., Danczyk, S.A., and Kastengren, A.L., Core Length and Spray Width Measurements in Shear Coaxial Rocket Injectors from X-Ray Radiography Measurements, *ILASS Americas: 27th Ann. Conf. Liquid Atom. Spray Syst.*, Raleigh, NC, May 2015.

Lin, K.-C., Kastengren, A.L., and Carter, C., Exploration of Temporal and Time-Averaged Two-Phase Flow Structures Using X-ray Diagnostics, *ILASS Americas: 29th Ann. Conf. Liquid Atom. Spray Syst.*, Atlanta, GA, May 15–18, 2017.

Linne, M., Analysis of X-ray Phase Contrast Imaging in Atomizing Sprays, *Exper. Fluids*, vol. **52**, no. 5, pp. 1201–1218, 2012a.

Linne, M., Analysis of X-ray Radiography in Atomizing Sprays, *Exper. Fluids*, vol. **53**, no. 3, pp. 655–671, 2012b.

Linne, M., Imaging in the Optically Dense Regions of a Spray: A Review of Developing Techniques, *Prog. Energy Combust. Sci.*, vol. **39**, no. 5, pp. 403–440, 2013.

Machicoane, N. and Aliseda, A., Experimental Characterization of a Canonical Coaxial Gas-Liquid Atomizer, *ILASS Americas 2017: 29th Ann. Conf. Liquid Atom. Spray Syst.*, Atlanta, GA, May 15–18, 2017.

Machicoane, N., Bothell, J.K., Li, D., Morgan, T.B., Heindel, T.J., Kastengren, A.L., and Aliseda, A., Synchrotron Radiography Characterization of the Liquid Core Dynamics in a Canonical Two-Fluid Coaxial Atomizer, *Int. J. Multiphase Flow*, vol. **115**, pp. 1–8, 2019.

Matusik, K.E., Sforzo, B.A., Seong, H.J., Duke, D., Kastengren, A., Ilavsky, J., and Powell, C.F., X-ray Measurements of Fuel Spray Specific Surface Area and Sauter Mean Diameter for Cavitating and Non-Cavitating Diesel Sprays, *Atom. Sprays*, vol. **29**, no. 3, pp. 199–216, 2019.

Moon, S., Gao, Y., Park, S., Wang, J., Kurimoto, N., and Nishijima, Y., Effect of the Number and Position of Nozzle Holes on in- and Near-Nozzle Dynamic Characteristics of Diesel Injection, *Fuel*, vol. **150**, pp. 112–122, 2015.

Morgan, T.B. and Heindel, T.J., An Automated System for Systematic Spray Expansion Angle Measurements," *ILASS-AMERICAS 2021, 31st Ann. Conf. Liquid Atom. Spray Syst.*, Virtual, May 16–19, 2021.

Mudde, R.F., Double X-ray Tomography of a Bubbling Fluidized Bed, *Indust. Engin. Chem. Res.earch*, vol. **49**, no. 11, pp. 5061–5065, 2010.

Osta, A.R., Lee, J., Sallam, K.A., and Fezzaa, K., Study of the Effects of the Injector Length/Diameter Ratio on the Surface Properties of Turbulent Liquid Jets in Still Air Using X-ray Imaging, *Int. J. Multiphase Flow*, vol. **38**, no. 1, pp. 87–98, 2012.

Rahman, N., Halls, B.R., James, J.W., McMaster, A., Lightfoot, M.D.A., Gord, J.R., and Meyer, T.R., 4D Imaging of Primary Liquid Breakup Using High-Speed Tomographic X-ray Radiography, *ICLASS 2018, 14th Tri. Int.l Conf. Liquid Atom. Spray Syst.*, Chicago, IL, July 22–26, 2018.

Settles, G.S. and Hargather, M.J., A Review of Recent Developments in Schlieren and Shadowgraph Techniques, *Meas. Sci. Technol.*, vol. **28**, no. 4, p. 042001, 2017.

Tekawade, A., Sforzo, B.A., Matusik, K.E., Fezzaa, K., Kastengren, A.L., and Powell, C.F., Time-Resolved 3D Imaging of Two-Phase Fluid Flow Inside a Steel Fuel Injector Using Synchrotron X-ray Tomography, *Sci. Rep.*, vol. **10**, no. 1, p. 8674, 2020.

Van Nieuwenhove, V., De Beenhouwer, J., De Carlo, F., Mancini, L., Marone, F., and Sijbers, J., Dynamic Intensity Normalization Using Eigen Flat Fields in X-ray Imaging, *Optics Express*, vol. **23**, no. 21, pp. 27975–27989, 2015.

Vu, L., Machicoane, N., Li, D., Morgan, T.B., Heindel, T.J., Aliseda, A., and Desjardins, O., Validation of Inflow Modeling Strategies for Numerical Simulations of Air-Blast Atomization against Experimental

Backlit Imaging and Radiographs, *ILASS-AMERICAS 2021, 31st Ann. Conf. Liquid Atom. Spray Syst.*, Virtual, May 16–19, 2021.

Zhang, G., Khlifa, I., and Coutier-Delgosha, O., A Comparative Study of Quasi-Stable Sheet Cavities at Different Stages Based on Fast Synchrotron X-ray Imaging, *Physics Fluids*, vol. **32**, no. 12, p. 123316, 2020a.

Zhang, G., Khlifa, I., Fezzaa, K., Ge, M., and Coutier-Delgosha, O., Experimental Investigation of Internal Two-Phase Flow Structures and Dynamics of Quasi-Stable Sheet Cavitation by Fast Synchrotron X-ray Imaging, *Physics Fluids*, vol. **32**, no. 11, p. 113310, 2020b.